

**Control of quantum interference frequency combs: Multistable temporal cavity solitons**Mansour Eslami <sup>1</sup>, Maedeh Sadat Hashemi,<sup>1</sup> David Grant,<sup>2</sup> and Gian-Luca Oppo <sup>2,\*</sup><sup>1</sup>*Department of Physics, University of Guilan, P.O. Box 41335-1914 Rasht, Iran*<sup>2</sup>*SUPA and Department of Physics, University of Strathclyde, Glasgow G4 0NG, Scotland, United Kingdom*

(Received 23 June 2023; accepted 1 November 2023; published 20 November 2023)

Two branches of bistable temporal cavity solitons are found in models of quantum interference in microresonators with a  $\Lambda$  three-level medium in the anomalous dispersion regime. The cavity solitons are due to the locking of moving domain walls. We identify two distinct Maxwell points on opposite sides of the cavity resonance where domain walls are stationary and two distinct temporal cavity solitons, one narrow and with a high peak intensity, the other broader and with a lower peak intensity, coexist over wide parameter ranges and without the need of secondary cavity resonances. Localized structures combining the two soliton branches oscillate on timescales of tens of cavity round trips. Frequency combs generated by combinations of different types of multistable temporal cavity solitons lead to enhanced bandwidths and their control.

DOI: [10.1103/PhysRevA.108.053511](https://doi.org/10.1103/PhysRevA.108.053511)**I. INTRODUCTION**

Temporal cavity solitons (TCSs) in a driven optical cavity are circulating pulses of light which maintain their shape against dispersion through medium nonlinearity. They have opened novel and interesting applications for all-optical memory, buffering, and pulse reshaping [1–5] and are used in both passive [6,7] and active [8–10] media to generate broad frequency combs. TCSs in microresonators have been particularly practical in harnessing phase coherence and providing broad and controllable generation of frequency combs with important applications from coherent high-speed communications and range measurements [11,12] to frequency standards and precise atomic clocks [13,14]. Optical microresonators have the ability to efficiently store and enhance light hence realizing nonlinear phenomena with dramatically low input powers. These topics have become the mainstream in recent photonics research due to the modern nanofabrication technologies that have realized optical microresonators with both a high quality factor and a small mode volume [15,16]. Operating regimes of normal Kerr frequency combs with stable dissipative temporal solitons are capable of providing a fully coherent optical comb while minimizing unwanted noise processes. These features have made TCS the preferred operating regime for the generation of Kerr frequency combs despite the challenges arising from thermal effects due to high-power pump lasers or transition steps from modulation instability to soliton states [17,18].

Nonlinear optical microcavities have also been remarkably successful in enabling quantum optical effects to be used

for quantum information processing and networks. Electromagnetically induced transparency (EIT) is one of the most notable quantum optics phenomena with new applications in optical switching devices, controlling the group velocity of light, and sensing and field enhancement [19–24]. EIT is a quantum interference phenomenon manipulating the optical response of a medium close to resonance where external electromagnetic fields cancel absorption and enhance the refractive index [25]. In the bare state picture, EIT is explained by destructive interference between probability amplitudes of the direct and indirect excitation pathways in a three-level (or more than three) system with a shared energy state. The indirect transition route to a second long-lived state acquires a phase shift of  $\pi$  in coupling from the upper state to the second metastable state and back. EIT resonance line shapes have been found in a variety of optical cavities [26] including microring resonators in silicon-on-insulator chips with air holes [27].

Optical cavities with three-level media displaying EIT have also been studied theoretically for the onset and stability of various transverse structures, from patterns to diffractive cavity solitons and even rogue waves and chimera states [28–33]. Recently, fast time EIT dynamics in microring resonators in the presence of group velocity dispersion have been investigated [34]. Using EIT in three-level media, one can substantially decrease absorption and input powers for frequency comb generation by avoiding difficulties associated with thermal effects. Quantum interference coupled with anomalous dispersion in microring resonators displaying EIT can lead to stable domain walls (DW), trapped stimulated Raman adiabatic passage (STIRAP [35]) schemes with no input pulses, bistable quantum dark states and novel TCS for frequency combs that do not require any modulation instabilities [34].

For three-level media in microring resonators there are several spatiotemporal features that remain to be studied. It is the aim of this paper to investigate the dynamics of DWs leading to different types of multistable TCSs. Bistable

\*g.l.oppo@strath.ac.uk

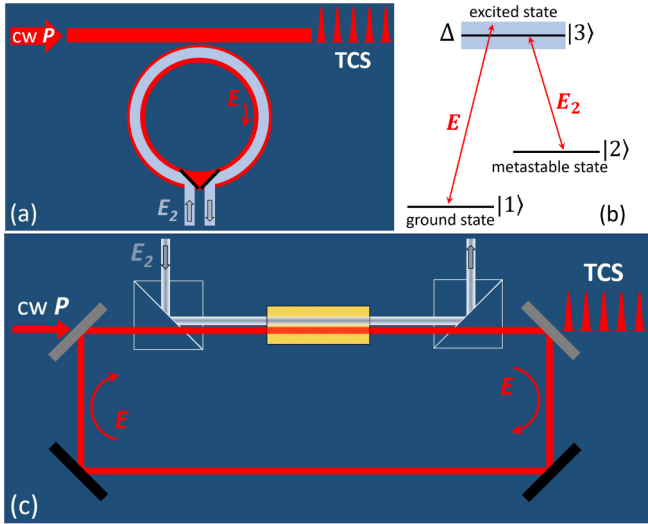


FIG. 1. (a) Schematic representation of a prototypical dispersive ring resonator device described by Eqs. (1) and (2). The black lines correspond to polarization beam splitters. (b) The  $\Lambda$  three energy level configuration. (c) Schematic representation of another dispersive resonator where the field  $E_2$  is not circulated in the cavity.

TCS can induce switching, dynamical transitions, controllable STIRAP efficiencies, and broadening of frequency combs. In Sec. II we discuss the details of the model equations and their steady-state properties. Maxwell points and dynamics of DWs close to their location in parameter space are presented in Sec. III. Multistable TCSs, their dynamics, switching, and the accompanying STIRAP effects are studied in Sec. IV. Different aspects of the resulting frequency combs are investigated in Sec. V while conclusions are drawn in Sec. VI followed by future outlooks.

## II. MODEL

We consider a prototypical microring resonator as displayed in Fig. 1(a) with an input from a straight waveguide at the top and an input at the bottom of the ring. The microresonator is filled with a three-level medium in the  $\Lambda$  configuration, as shown in Fig. 1(b), where states  $|1\rangle$  and  $|2\rangle$  are the ground states and state  $|3\rangle$  is an excited state. The transitions  $|1\rangle \rightarrow |3\rangle$  and  $|2\rangle \rightarrow |3\rangle$  are dipole-allowed transitions while  $|1\rangle \rightarrow |2\rangle$  is dipole-forbidden. The field  $E$  circulates in the ring cavity under the external cw driving proportional to  $P$  and couples states  $|1\rangle$  and  $|3\rangle$ . Note that the field  $E$  is considered here to be blue detuned by  $\Delta$  from the resonance of levels  $|1\rangle$  and  $|3\rangle$ . The coupler at the top of the ring resonator in Fig. 1(a) is only for field  $E$  with a high reflectivity and low transmittivity. By using polarization beam splitters [black lines in Fig. 1(a)] the field  $E$  keeps circulating in the cavity while the field  $E_2$  of opposite polarization is flushed out of the cavity every round trip. The control field  $E_2$  couples states  $|2\rangle$  and  $|3\rangle$  and is not recirculated in the ring cavity. In this way, any small change to the field  $E_2$  during a round trip is forgotten. This means that in the mean-field approximation the field  $E_2$  inside the ring resonator is the same as the cw pump  $E_2$  at all times. Note that field  $E_2$  is not affected by the coupler at the top of Fig. 1(a) because the frequencies of

$E$  and  $E_2$  are quite different from each other [see Fig. 1(b)]. For completeness, we show in Fig. 1(c) another ring resonator configuration with a three-level medium where the field  $E_2$  interacts with  $E$  in the medium, but is not circulated in the cavity. This configuration has been experimentally implemented in [36] to control optical bistability in rubidium atoms. In the case of a medium with a fast response and anomalous group-velocity dispersion, the dynamics of the field  $E$  in the ring resonator is described by the mean-field equation [37]

$$\partial_t E = P - (1 + i\theta)E + i(2C)R_{13} + i\partial_{\tau^2} E, \quad (1)$$

where  $t$  is the slow time over several round trips in the cavity,  $P$  is the amplitude of the input pump,  $\theta$  is the cavity detuning from the input frequency, and  $2C$  is the cooperativity parameter of the light-matter coupling that is proportional to the square of the dipole moment of the transition between levels  $|1\rangle$  and  $|3\rangle$ . All physical quantities that appear in Eq. (1) have been made dimensionless by suitable normalizations following standard procedures for the derivation of models of the Lugiato-Lefever type [37]. In [28–33] we focused on the transverse diffractive case while here we investigate the case of anomalous group velocity dispersion through a longitudinal variable  $\tau$ , the fast time in the cavity.  $R_{13}$  is the density matrix element in the Lindblad master equation given by [28,38]

$$R_{13} = \chi(|E|^2)E = -\frac{\Delta|E_2|^2(|E_2|^2 + |E|^2 - \Delta^2 - i\Delta)}{D}E, \\ D = (|E_2|^2 + |E|^2)^3 + \Delta^2(|E_2|^2 + |E|^2 + 4|E_2|^2|E|^2 + \Delta^2|E_2|^2 - 2|E_2|^4). \quad (2)$$

Again, all quantities are dimensionless by appropriate normalizations.

Medium and cavity decays are considered within the Lindblad and mean-field approaches, while thermal excitations from a lower to a higher level can be safely neglected as long as the energy separation between levels is much larger than the thermal energy available to the system at room temperature. For the numerical simulations presented below, expression (2) is not strictly necessary and can be replaced by any numerical solver of algebraic equations that provide the steady states of the density matrix equations given in [38] as done, for example, in [28]. Here we use the cavity detuning  $\theta$  as the control parameter while keeping the values of medium detuning  $\Delta$ ,  $|E_2|^2$ , and  $2C$  fixed unless stated otherwise. In the case of a fast medium response, the medium linewidth is large, but the EIT bandwidth remains quite narrow [24] and operations with EIT advantages require a careful choice of the input frequency that fixes the medium detuning  $\Delta$ . Contrary to two-level systems where operations are far from medium resonance and tuning is generally obtained by changing the input laser frequency [13], we use changes in  $\theta$  by operating on cavity features with no consequences on the value of  $\Delta$  and input frequency which can be kept fixed in the simulations. Although scanning the cavity detuning without changing the input frequency is uncommon in Kerr resonators, cavity tuning through changes in length or temperature are standard techniques in nonlinear optics and laser physics and have been implemented recently in ring resonators via fiber-spools stretched by piezoelectrical crystals [39] or micro [40] and Peltier [41] heaters, respectively. The intensities  $|E_s|^2$  of the homogeneous stationary

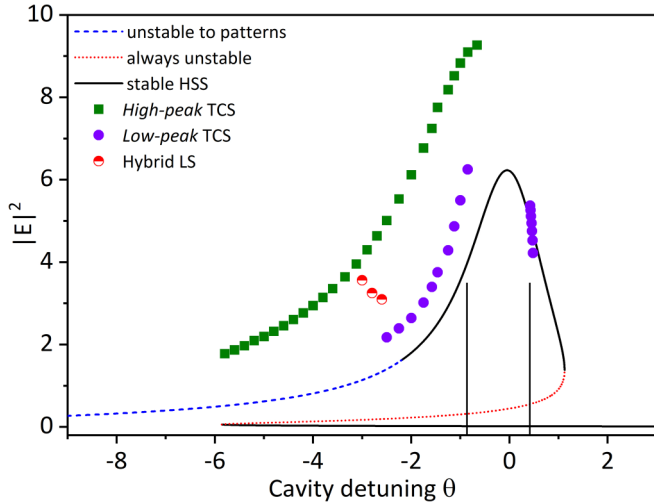


FIG. 2. HSS and branches of TCS in cavity detuning scans. Black-solid (red-dotted) lines correspond to stable (unstable) HSS and blue-dashed line to HSS unstable to patterns. Green squares (purple circles) correspond to *high-* (*low-*) *peak* TCS while red-white circles to multip peaked dynamical TCS, labeled as hybrid localised states. The reported values for these structures correspond to the largest peak intensity of the solitons. The two vertical lines identify the detuning values of the Maxwell points. Other parameter values are  $P = 2.5$ ,  $\Delta = 0.2$ ,  $|E_2|^2 = 0.3$ , and  $2C = 35$ . The cavity detuning  $\theta$  and the output intensity  $|E|^2$  are considered to be dimensionless quantities throughout the paper.

solutions (HSS) are obtained from Eq. (1) by setting  $\partial_t = 0$  and  $\partial_t^2 = 0$ :

$$|P|^2 = \{[1 + 2C \operatorname{Im}(\chi)]^2 + [\theta - 2C \operatorname{Re}(\chi)]^2\} |E_s|^2, \quad (3)$$

where  $\operatorname{Re}(\chi)$  and  $\operatorname{Im}(\chi)$  are the real and imaginary parts of the complex susceptibility in Eq. (2). HSS are shown in Fig. 2 when changing the cavity detuning  $\theta$ . Here we observe a clear optical bistability close to cavity resonance where the red-dashed HSS is unconditionally unstable. In contrast to [34], the bistable region is not a closed bubble but a heavily curved S-shaped region due to the selected value of  $|E_2|^2$ . The stability of HSS can be obtained by standard linearization techniques and it is found that the high-intensity HSS branch is stable for  $\theta > -2.15$  and unstable to modulated perturbations (patterns) for  $-18.2 < \theta < -2.15$ . This is depicted by the blue dashed line in Fig. 2.

### III. MAXWELL POINTS AND DOMAIN WALLS

On both sides of the cavity resonance, we observe bistability of the low and high intensity branches of the HSS. There are solutions that connect the low-intensity branch to the high-intensity branch and vice versa during a round trip of the cavity. In the absence of an exchange symmetry, kinks connecting the two bistable states are labeled as switching waves [42,43]. Although not immediately evident as the field  $E_2$  is not resonated, our model is invariant under the exchange of the level indices 1 and 2. For this reason, the kinks in our system are better labeled as domain walls (DW) [44] in analogy with magnetic systems. Switching waves and DWs were studied in nonlinear optics in various systems, see, for

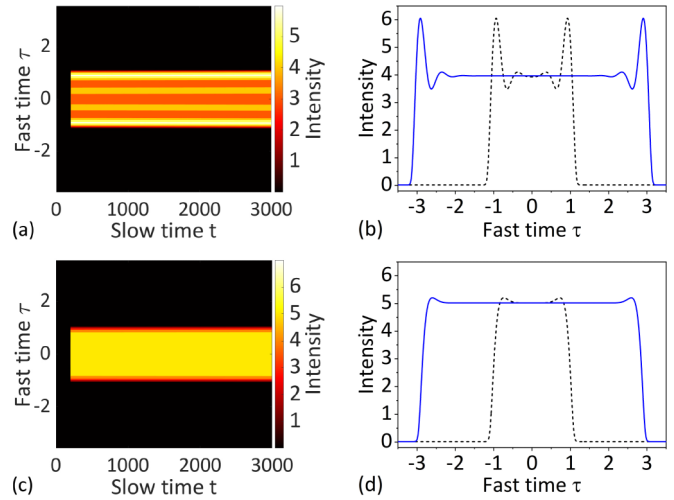


FIG. 3. (a) Slow time evolution of stationary DWs excited at the first Maxwell point  $\theta_M^{(1)} = -0.8645$  and (b) two examples of asymptotic intensity profiles. (c) Slow time evolution of stationary DWs excited at the second Maxwell point  $\theta_M^{(2)} = +0.41535$  and (d) two examples of asymptotic intensity profiles. Other parameter values as in Fig. 2.

example, [43–51]. They connect one HSS to another in regimes of optical bistability. For precise values of the detuning  $\theta$  the areas corresponding to the two HSS equilibrate and the DWs connecting these two solutions do not move in time. These are the so called “Maxwell” points in analogy with the Maxwell construction for gas-liquid phase transitions when the two phases balance each other. Away from the Maxwell points, DW travel and domains of one HSS solution expand into the regions occupied by the other. The velocity and the direction of the DW motion depend on the control parameters of the systems, here the cavity detuning  $\theta$ .

Differently from what we presented in [34], we locate and study two Maxwell points, characterized by zero velocity of the DWs, when tuning the cavity detuning  $\theta$ . In the vicinity of Maxwell points, the DWs are able to create different localized structures because of the local fast-time oscillations clearly visible in Fig. 3 close to the high power HSS. The two Maxwell points here are labeled  $\theta_M^{(1)}$  and  $\theta_M^{(2)}$  and reside on the two sides of the cavity resonance where upward and downward DWs exist and are stationary at many separation distances, see, for example, Fig. 3 where we consider realistic microresonators with a free spectral range of around 140 GHz, input powers of few mWs, and realistic detunings in agreement with realizations of silicon-on-insulators devices [52]. When referring to realistic microresonators, the fast timescale  $\tau$  reported in the figures throughout the paper can be thought of as being in the range of picoseconds. It is important to note that the tail oscillations are enhanced in DWs close to the negative Maxwell point  $\theta_M^{(1)} = -0.8645$  compared to those close to the positive Maxwell point  $\theta_M^{(2)} = 0.41535$  and those reported in [34]. As we shall see later, this makes it possible for the DWs to lock at the different minima of the oscillating tails and form different TCSs. Therefore, the resulting bistable TCSs are neither supported in the positive side of the resonance close to the second Maxwell point  $\theta_M^{(2)}$  nor in the parameter regions used in [34].

When moving across a DW inside the resonator, the highest probability of occupancy goes from state  $|1\rangle$  (low output intensity) to state  $|2\rangle$  (high output intensity) while the probability of occupancy of level  $|3\rangle$  remains well below 1% due to CPT and EIT. The probabilities of occupancy of the three levels  $R_{11}$ ,  $R_{22}$ , and  $R_{33}$  can be obtained from the analytical expressions given in the Appendix, and the field  $E$  provided by the HSS. Simulations in [34] show that more than 90% of the population of level  $|1\rangle$  can be transferred to level  $|2\rangle$  when moving from one side of the DW to the other in a process that we can label as *DW-enhanced STIRAP* which comes as a result of the nonlinear response of the cavity and should be distinguished from the conventional STIRAP due to gated pulses in three-level media. STIRAP allows efficient and selective population transfer between quantum states without suffering loss due to spontaneous emission since it is prevented from the intermediate state by quantum interference [35]. STIRAP has found widespread applications in science and engineering [53] and is based on a sequence of two gated pulses of laser light with appropriate Rabi frequency (i.e., intensity) profiles. The DW-enhanced STIRAP presented here requires no pulsed light at the input, and once formed by initial perturbations of the HSS, it keeps circulating in the resonator. During this round trip, one part of the resonator resides in one of the two (dark) quantum states while the other part is in the second of the two (dark) quantum states. We will see later the possible manipulation of the STIRAP process when dealing with two families of TCS.

Away from the values of the cavity detuning  $\theta_M^{(1)}$  and  $\theta_M^{(2)}$  corresponding to the Maxwell points where the DWs maintain a fixed distance, traveling DWs are found with velocities and directions (i.e., towards or away from each other) depending on the value and sign of  $\theta$ . For  $\theta_M^{(1)} < \theta < \theta_M^{(2)}$ , DWs move away from each other while for  $\theta < \theta_M^{(1)}$  and for  $\theta > \theta_M^{(2)}$  DWs approach each other. For each value of the detuning  $\theta$  the DWs velocity  $\mathcal{V}$  is constant during motion and can be measured by evaluating the changing distance between two DWs in the slow time. We consider a positive value of the velocity when two DWs approach each other and a negative value when they move away. The velocities of the traveling DWs (in femtoseconds per round-trip time) are shown in Fig. 4 for various values of the detuning  $\theta$ . The zero crossings correspond to the locations of the Maxwell points where the direction of motion flips. Intensity profiles of expanding or shrinking domains between two DWs are shown in Fig. 5 for regions 1 to 4 of Fig. 4 where the sign of the DW velocity changes as explained above.

#### IV. MULTISTABLE TEMPORAL CAVITY SOLITONS AND STIRAP EFFICIENCY

Since our optical DWs display local fast time oscillations due to group-velocity dispersion, for cavity detunings  $\theta$  for which DWs travel towards each other, two DWs can lock with each other and form stable stationary TCS without requiring modulational instabilities and in a way similar to what was described for optical parametric oscillators [45,46] and second harmonic generation [51]. Locking can also take place when DWs travel away from each other since the resonator has a finite length. In this case they may form dark TCSs due to

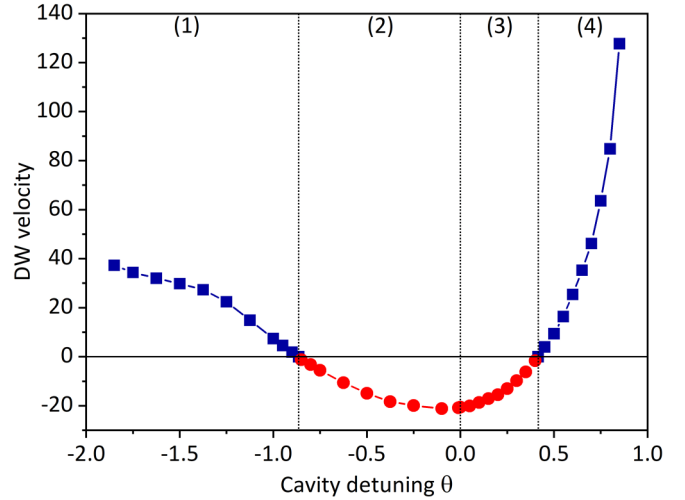


FIG. 4. Velocities of the DWs (femtoseconds/round trip time) in a cavity detuning scan. Stationary DWs at the two Maxwell points can be seen in the zero crossing of the curves. Other parameter values as in Fig. 2.

local oscillations close to the bottom of the DWs. In our model these dark TCSs can be stable in very small parameter regions and will be discussed elsewhere. The fact that our TCSs do not require modulational instabilities to form is very useful to avoid unwanted thermal effects due to sudden changes in circulating intracavity power as it happens for dissipative Kerr solitons for two-level media [6]. In these cases, the seeding and excitation of the TCS can lead to large thermal resonance shifts during the excitation process and render the soliton states short lived. This is detrimental for TCS in two-level media with anomalous dispersion since they can only exist over a restricted detuning range since a changing thermal

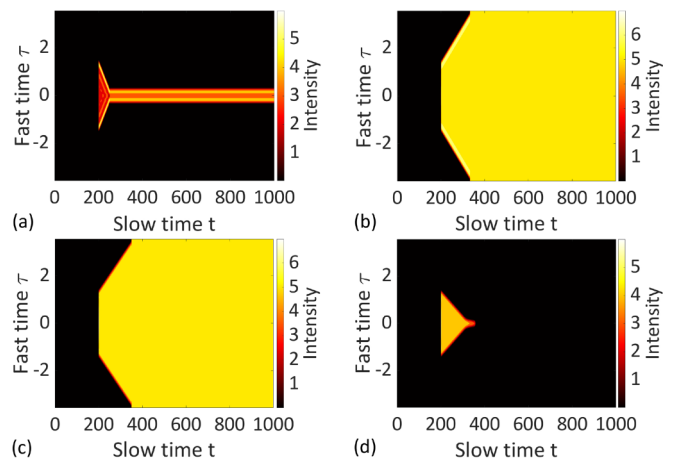


FIG. 5. Moving DWs in regions labeled 1 to 4 in Fig. 4. (a) DWs approach each other and lock to form a *low-peak* TCS for  $\theta = -1.25$  inside region 1. DWs move away from each other and the entire structure switches to the upper HSS for (b)  $\theta = -0.5$  and (c)  $\theta = +0.25$  inside regions 2 and 3. (d) DWs approach each other but they do not lock for  $\theta = +0.5$  inside region 4. Note that DWs stably lock and form a temporal cavity soliton for  $\theta_M^{(2)} < \theta < 0.480$  similar to (a). Other parameter values as in Fig. 2.

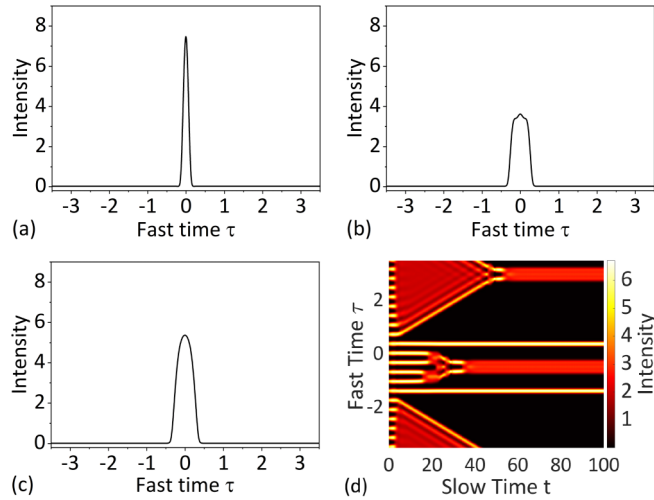


FIG. 6. Intensity profile of (a) a *high-peak* TCS and (b) a *low-peak* TCS at  $\theta = -1.5$  and (c) a *low-peak* TCS at  $\theta = +0.42$ . (d) Slow time evolution of the intensity at  $\theta = -1.8$  of a periodic pattern solution initially obtained at  $\theta = -2.3$ . Other parameter values as in Fig. 2.

shift accompanies a displaced detuning. Power kicking and other practical techniques have been introduced to overcome the effects of modulational instabilities and thermal effects in accessing Kerr soliton states [17,18,54]. None of these are necessary for the TCS due to quantum interference described here since the dynamics leading to their formation is purely deterministic, robust to fluctuations and does not induce any thermal shift.

For  $\theta = -1.5$ , pump amplitude 2.5 and a stable low HSS equal to  $2.02 \times 10^{-2}$ , we use an initial Gaussian perturbation of amplitude 5 and width 3.084 ps and observed the low-intensity HSS expanding into the region of high-intensity HSS until the DWs lock and form a quantum interference TCS, see Fig. 6(a). By using instead an initial Gaussian perturbation of a similar amplitude but much smaller width (0.046 ps) a different TCS is formed, see Fig. 6(b). In view of the different peak height of these two bistable localized states, we label the first (second) one as *high-peak* (*low-peak*) TCS. These two stable TCSs correspond to DWs locking at different minima of the oscillating tails [45,46,55]. On the positive side of the cavity resonance, there is only one type of TCS which has a peak intensity close to that of the *low-peak* TCSs observed at negative cavity detunings, see Fig. 6(c). Of the three different TCS branches reported here, it is only the *high-peak* TCSs that are analogous to those discussed in [34] where enhanced local tail oscillations and a second Maxwell point on the positive side of the cavity resonance are missing. Figure 6(d) shows how sequences of *high-peak* and *low-peak* TCSs can originate spontaneously. By quickly changing the cavity detuning from  $-2.3$  to  $-1.8$ , a periodic pattern breaks up into two *high-peak* and two *low-peak* TCSs that remain stable in the long time. The motion of the DWs is also clearly visible. In Fig. 7 we show two bistable TCS during a single cavity round trip and the long term stability of such configuration.

Figure 8 shows the bands of excitation of single *high-* and *low-peak* TCSs as a function of the cavity detuning and the perturbation amplitude. In the region labeled “Multiple

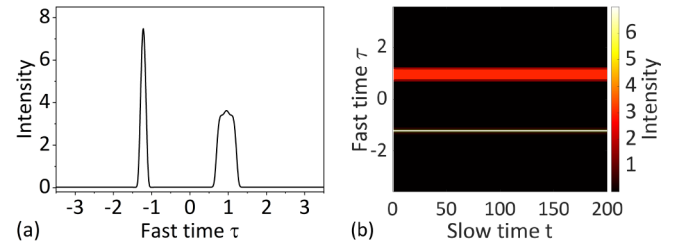


FIG. 7. (a) Intensity profile of a *high-peak* and *low-peak* TCS sequence for  $\theta = -1.5$ . (b) Slow time stability of the TCS sequence. Other parameter values as in Fig. 2.

high-peak TCS,” two or three (or more) *high-peak* TCSs are created but not single (high or low) peak TCS. These are reminiscent of the so-called soliton crystals [56]. To understand better the coexistence of the two types of multistable TCSs on the negative side of the cavity resonance and their switching we sketch in Fig. 9 the phase-space dynamics for successful excitation of these two TCSs for  $\theta = -2.38$  by proper perturbation amplitudes shown in Fig. 8. It is seen that the trajectories starting from the same homogeneous state converge to two different attractors belonging to *low-peak* and *high-peak* TCSs depending on the perturbation amplitude of the initial condition. The branches of *high-* and *low-peak* TCSs on the left side of the cavity resonance and that of *low-peak* TCSs on its right side are shown in Fig. 2. It is remarkable that the bistable TCS exists in a region where there is bistability of HSS as well. When scanning the detuning from negative values to resonance, one first observes a single HSS (later the high intensity HSS) that is unstable to Turing patterns. Then two new HSS are created through a saddle-node bifurcation around  $\theta = -6$ . The newly created low-intensity HSS is stable and provides the base for the high-peak TCS through the mechanism of bistable homogeneous

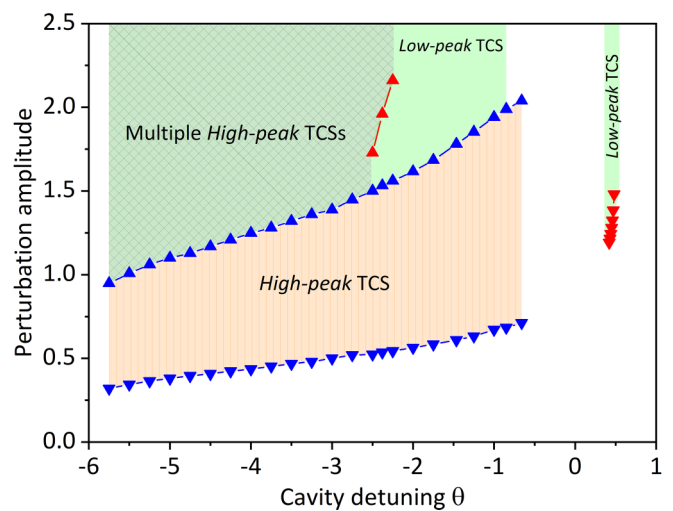


FIG. 8. Gaussian perturbation amplitude required for exciting *high-* and *low-peak* TCSs normalized to the input pump amplitude. Multiple TCSs can be excited from homogeneous solutions beyond the intermediate dynamical region (up red triangles) for  $\theta \leq -2.5$ . The width of the Gaussian perturbation is 0.046 ps. Other parameter values as in Fig. 2.

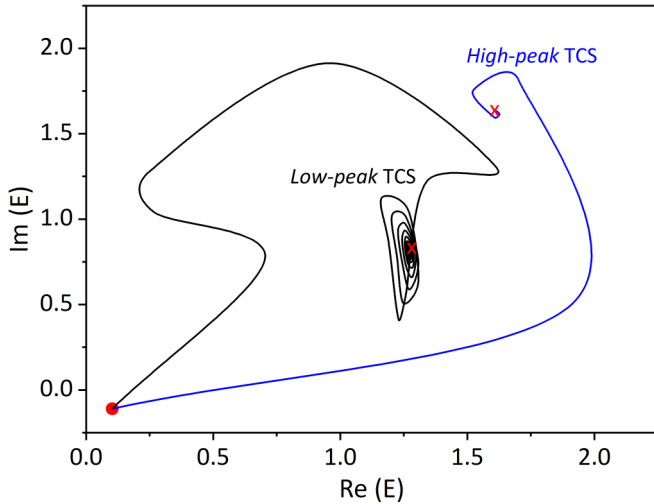


FIG. 9. Phase-space trajectories during excitation of multistable TCSs at  $\theta = -2.38$ . The initial homogeneous state is shown by a red circle and the final states belonging to *high-* and *low-peak* TCSs are marked by red crosses. Perturbation amplitudes are 1.35 and 3.9 for switching *high-* and *low-peak* TCSs, respectively, with a fixed width of 0.046 ps. Other parameter values as in Fig. 2.

and Turing pattern states as described in [57]. This kind of TCS is typical of anomalous dispersion regimes. At around  $\theta = -2.15$  the high intensity HSS gains stability while the high-peak TCS remains stable. A new TCS [the low-peak TCS, see Fig. 6(b)] due to the locking of the DWs is now created around the stable high intensity HSS. For a wide range of detuning values one observes TCS bistability.

TCS multistability is an uncommon phenomenon and makes it possible to have access to two families of separate localized states with different temporal shapes and spectral profiles at the same values of the control parameters and conditions of operation. Multistability of cavity solitons for a nonlinear cavity under quantum coherence and the action of diffraction instead of dispersion was reported in [32]. Multistability and coexisting solitons were also studied in [58–60] where a second family of soliton solutions (also known as supersoliton) due to the nonlinear bending of the response over the next cavity resonance was included (by either using an Ikeda map [58,59] or an augmented Lugiato-Lefever equation [60]). A multistable regime that supports two types of bistable cavity solitons was also reported in a doubly resonant and dispersive cavity system phase-matched for third-harmonic generation [61]. Note that our bistable TCS are due to the locking mechanism of DW's oscillating tails, to quantum interference with small medium and cavity detunings and do not require secondary cavity resonances. As well as bistable single peak TCSs, we also observe intermediate localized structures between the *high-* and *low-peak* TCS branches (see red half-filled circles in Fig. 2). Starting from a *low-peak* TCS and moving to more negative values of the cavity detuning, the single-peak TCS widens and gradually develops two other peaks on its sides, see Figs. 10(a) and 10(b) corresponding to  $\theta = -2.0$ . The appearance of side peaks leads to an oscillating hybrid localized structure formed by alternating a *high-peak* TCS with side peaks and a two-*high-peak* localized

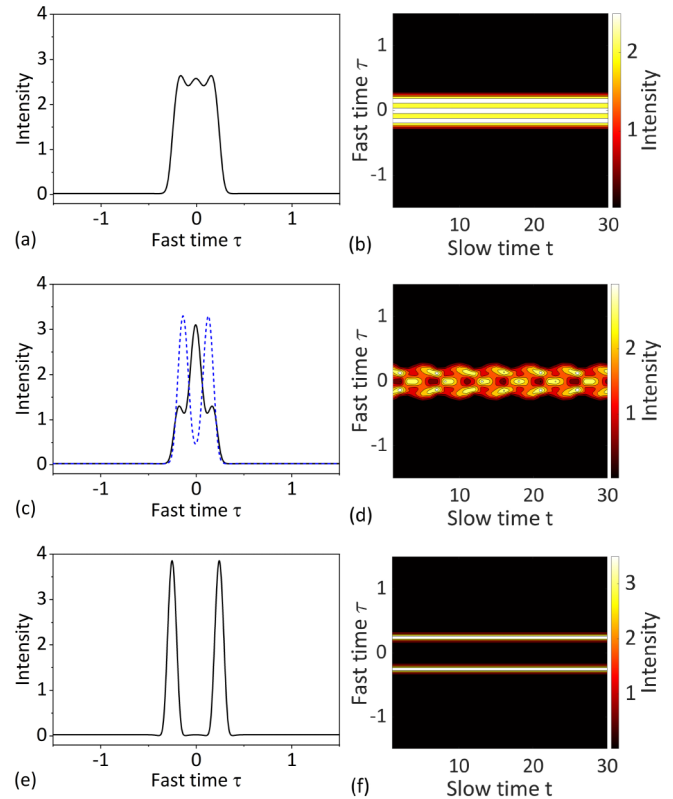


FIG. 10. Fast time intensity profiles of (a,b) a broad *low-peak* TCS for  $\theta = -2.0$ , (c,d) from single to double peak and back dynamics for  $\theta = -2.6$  and (e,f) stable twin *high-peak* TCS for  $\theta = -3.2$ . Other parameter values as in Fig. 2.

structure as shown in Figs. 10(c) and 10(d) corresponding to  $\theta = -2.6$ . Oscillatory localized structures continue until one encounters the *high-peak* TCS branch at  $\theta = -3.0$  where two well-separated *high-peak* TCSs are observed, see Figs. 10(e) and 10(f). Once formed, these two well-separated *high-peak* TCSs move apart from each other due to the interaction of the exponentially decaying tails until an equilibrium distance is found. These repulsive interactions of the two soliton peaks are robust and present for detuning values down to  $\theta = -5.80$  where Turing patterns set in. We note that repulsive interactions of TCS with exponentially decaying tails were found in passively mode-locked lasers [62].

At the end of the dynamic region, twin *high-peak* TCSs follow the *high-peak* TCS branch. It is interesting to see that for a region of parameter space between  $\theta = -3.0$  and  $\theta = -2.55$  *high-peak* TCSs are bistable with oscillating localized structures that branch out from the *low-peak* TCS branch. As a matter of fact, when decreasing the cavity detuning there exists a Hopf bifurcation of the single *low-peak* TCS at  $\theta = -2.554$ . Around  $\theta = -2.6$  this oscillation morphs into an oscillating hybrid structure formed by alternating single and double-peak solitons as shown in Figs. 10(c) and 10(d).

To complete the investigation of the bistable TCS we report in Fig. 11(a) the full-width-at-half-maximum (FWHM) sizes of quantum interference TCSs over the intervals of TCS existence in the cavity detuning parameter  $\theta$ . These values are in the subpicosecond regime when using realistic comparison to real devices [52] as specified in [34]. By using the expressions

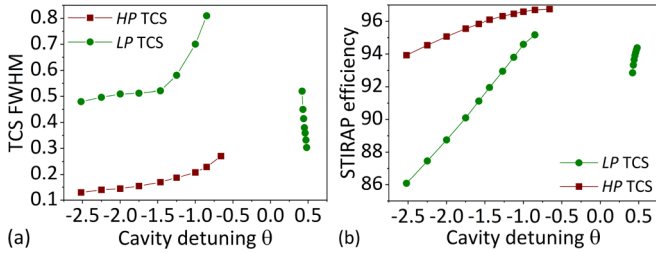


FIG. 11. (a) Full-width-at-half-maximum sizes of TCSs at the two sides of the cavity resonance in  $\theta$  scans. (b) STIRAP efficiency values (in percentage) in the cavity detuning  $\theta$  scan. *HP* and *LP* stand for *high-peak* and *low-peak*, respectively. Other parameter values as in Fig. 2.

in the Appendix, it is possible to evaluate the probabilities of occupancy of the three energy levels once the intensity profiles of the TCS are specified. The formation of TCS by locking of moving domain walls leads to an underlying STIRAP process corresponding to the transfer of probability of occupancy from level  $|1\rangle$  to level  $|2\rangle$  and vice versa. In Fig. 11(b) we show that the efficiency of the STIRAP process is between 86% and 97% for the TCS presented here since the probability of occupancy of state  $|1\rangle$  is very high in the TCS tails and the probability of occupancy of state  $|2\rangle$  is very high at the TCS peaks. We observe that *high-peak* TCSs close to cavity resonance feature the highest STIRAP efficiencies that are accessible without any complicated use of gated pulses, phase fluctuation managements, or balancing of two-photon resonances.

## V. QUANTUM INTERFERENCE IMPLEMENTATION OF FREQUENCY COMBS

Quantum interference TCSs formed by locked DWs have a very high contrast (visibility) since their tails are anchored on the lower HSS branch corresponding to very low intensities of the light. We also observe that there are almost no local modulations at the bottom of the TCS peaks making them quite different from typical TCSs in two-level Kerr resonators in the anomalous dispersion regime and excellent candidates for the generation of frequency combs. Figure 12 shows three examples of frequency combs for the multistable *high-* and *low-peak* TCSs at  $\theta = -2.0$  and the *low-peak* TCS at  $\theta = +0.45$ . The *high-peak* TCS [Fig. 12(a)] has a high intensity definition resulting in a broad spectrum while the *low-peak* TCS at the same cavity detuning value [Fig. 12(b)] displays a lower peak intensity and a wider width resulting in a narrower spectrum. The frequency combs of TCS on the positive side of the cavity resonance [Fig. 12(c)] also display spectra that are narrower than those corresponding to *high-peak* TCS. The modulations appearing on the sides of the spectra of our TCS are due to the mechanism of locking of DWs that results in phase distributions not following the amplitude profiles of the solitons.

The bandwidth of frequency combs generated by quantum interference dark states is shown in Fig. 12(d). The frequency comb spectrum provided by the *high-peak* TCSs with negative cavity detuning is much broader than their *low-peak* counterparts on both sides of the cavity resonance. It is interesting

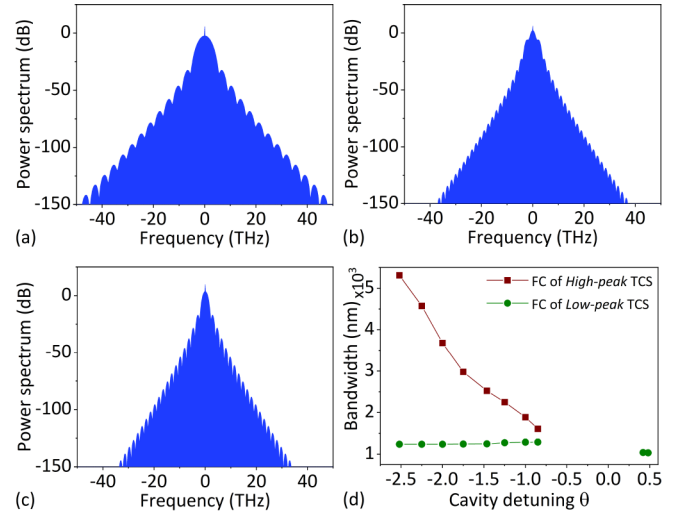


FIG. 12. Spectrum of the locked DW TCSs for (a) *high-peak* and (b) *low-peak* states of  $\theta = -2.0$ , and (c) the only TCS type (*low-peak*) of the  $\theta = +0.45$  after subtraction of the carrier frequency of the input light. (d) The bandwidth of frequency combs obtained from different types of multistable TCSs in a cavity detuning scan. FC stands for frequency comb. Other parameter values as in Fig. 2.

to note that multistable TCS branches in our system make it possible for the operator to choose between two frequency combs of remarkably different bandwidth, i.e., one can realize much broader bandwidths by choosing a *high-peak* instead of a *low-peak* TCS with all system parameters (e.g., cavity detuning) unchanged.

A further advantage of operation in the bistable TCS regime is that of creating soliton crystals or soliton glass made of regular or irregular sequences of the *high-* and *low-peak* TCS, respectively. For the basic *high-* and *low-peak* configuration of TCS, see Fig. 7(a), the frequency comb displayed in Fig. 13(a) clearly maintains the broad width of the spectrum of the single *high-peak* TCS while doubling the number of teeth in the comb. This is similar to the comb generated by two *high-peak* TCS but with the possibility of coding messages in the sequence of high-low peaks. In standard microresonators with two-level media and a periodic intracavity potential field, regularly spaced soliton crystals with up to 32 TCS were demonstrated [56]. In our quantum interference case it should be possible to have crystals of 64 TCS with chosen sequences

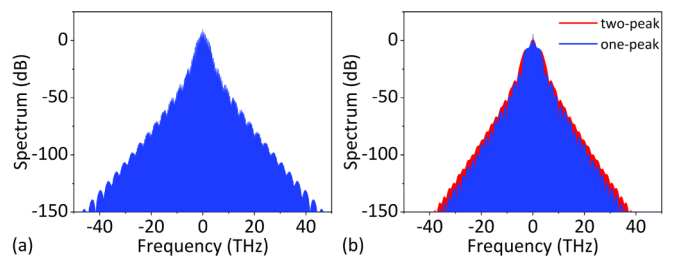


FIG. 13. (a) Spectrum of the two-peak configuration of Fig. 7 for  $\theta = -1.5$ . (b) Spectrum the dynamical configuration of Fig. 10 for  $\theta = -2.6$ . The red region is due to the two-peak structure. Other parameter values as in Fig. 2.

of the high and low TCS capable to communicate coded messages.

Finally, we show in Fig. 13(b) the frequency comb generated when operating in the slowly oscillating localized structure displayed in Fig. 10 for  $\theta = -2.6$ . Since the dynamics alternates between a two-peak and a single-peak configuration, it is possible to identify in the spectrum the components of each these structures. The red region of the frequency comb shown in Fig. 13(b) is due to the two-peak structure while the narrower frequency comb (in blue) is due to the single-peak structure. The coexistence of four separate frequency combs due to the *high-peak* TCS, *low-peak* TCS, their alternation in the fast time, and their oscillations in the slow time shows the richness of possible behaviors of the quantum interference processes in our system.

## VI. CONCLUSION

We discussed dynamical DWs and TCSs formed by locked DWs as localized quantum interference structures which are robust to perturbations, have a wide range of existence and stability, and, at difference from stable DWs observed experimentally for two-level media with normal dispersion [43,44], allow one to operate in the anomalous dispersion regime. Quantum interference DWs and TCSs do not require modulational instabilities, in contrast to their two-level Kerr counterparts, providing ease of access to soliton states without dealing with undesirable thermal shifts affecting the soliton existence range [17,18]. We showed that quantum interference is responsible for the generation of stable DWs and TCSs on both sides of the cavity resonance due to the locking of DWs in the vicinity of the two separate Maxwell points in microresonators driven by two external fields close to the medium resonances and in the presence of anomalous group velocity dispersion.

We demonstrated that TCSs via quantum interference and anomalous dispersion can exist in the presence of two stable homogeneous states, display very low absorption, and enhance nonlinear features due to EIT. In particular, we introduced here two different types of bistable TCSs referred to as *low-peak* and *high-peak* TCSs with distinct properties and consequences on the generation of frequency combs over wide ranges of the detuning variations. Their unusual coexistence is due to the locking of fronts with oscillatory tails at separate distances. *High-peak* TCSs provide frequency combs much broader than their *low-peak* counterparts at the same values of the control parameters due to their higher intensities and narrower widths. As well as the optimal shape of the TCSs due to quantum interference for the generation of microresonator frequency combs, their bistability enables the operator to choose

the desired bandwidths without need of changing system parameters. We identified, for example, a regime where four different frequency combs due to multistable configurations of TCS are possible. One advantage of our bistable regime of operation is the possibility of generating not only sequences of TCS all of the same kind, but also of an alternating kind and even randomly distributed solitons of one kind in sequences of the other. In practical applications this should allow for the realization of soliton crystals with random impurities due to the rare occurrence of the second type of solitons. In the bistable regime described here, two kinds of crystals with impurities are possible, one with periodic *high-peak* TCSs and random *low-peak* TCSs and the other with periodic *low-peak* TCSs and random *high-peak* TCSs. The number of different soliton sequences at the disposal of the operator is huge with great advantages in coding of signals and optical communications.

We also discussed dynamical states formed by single- and double-peak localized states and frequency combs generated by sequences of quantum interference TCSs and dynamical states. It is remarkable to see that our bistable TCS due to quantum interference and EIT do not require secondary cavity resonances as used for supersolitons in [58–60].

There are still many open topics of interest in this area of research such as oscillations in slow-time dynamics, the effect of detuned and intense  $E_2$  fields leading to Fano-like resonances, cavities where both fields  $E_1$  and  $E_2$  are resonated, normal dispersion configurations, as well as quantum interference in  $V$  and ladder three-level media in ring resonators which are presently under investigation.

## APPENDIX: PROBABILITIES OF OCCUPANCY OF ENERGY LEVELS

Given HSS values of the field intensity  $|E_s|^2$  the probability of occupancy of each of the three levels are given by

$$\begin{aligned} R_{11} &= 1 - R_{22} - R_{33}, \\ R_{22} &= \frac{|E_s|^2[ (|E_s|^2 + |E_2|^2)^2 + \Delta^2(1 + |E_2|^2) ]}{D}, \\ R_{33} &= \frac{2\Delta^2|E_s|^2|E_2|^2}{D}, \end{aligned} \quad (\text{A1})$$

where  $D$  is the denominator appearing in Eq. (2). Since we are working at small values of the medium detuning  $\Delta$  coherent population trapping (CPT) leads to extremely low values of the probability of occupancy of the excited state  $|3\rangle$  ( $R_{33}$ ) below 0.035 in the parameter regions explored in this paper. In principle, this value can be made even lower by maneuvering over the parameter values, see, for example, [34].

[1] F. Leo, S. Coen, P. Kockaert, S.-P. Gorza, P. Emplit, and M. Haelterman, Temporal cavity solitons in one-dimensional Kerr media as bits in an all-optical buffer, *Nat. Photonics* **4**, 471 (2010).  
 [2] D. Y. Tang, J. Guo, Y. F. Song, G. D. Shao, L. M. Zhao, and D. Y. Shen, Temporal cavity soliton formation in an anomalous dispersion cavity fiber laser, *J. Opt. Soc. Am. B* **31**, 3050 (2014).

[3] J. K. Jang, M. Erkintalo, S. Coen, and S. G. Murdoch, Temporal tweezing of light through the trapping and manipulation of temporal cavity solitons, *Nat. Commun.* **6**, 7370 (2015).  
 [4] J. K. Jang, M. Erkintalo, S. G. Murdoch, and S. Coen, Writing and erasing of temporal cavity solitons by direct phase modulation of the cavity driving field, *Opt. Lett.* **40**, 4755 (2015).  
 [5] J. K. Jang, M. Erkintalo, J. Schröder, B. J. Eggleton, S. G. Murdoch, and S. Coen, All-optical buffer based on temporal

- cavity solitons operating at 10 Gb/s, *Opt. Lett.* **41**, 4526 (2016).
- [6] T. Herr, V. Brasch, J. D. Jost, C. Y. Wang, N. M. Kondratiev, M. L. Gorodetsky, and T. J. Kippenberg, Temporal solitons in optical microresonators, *Nat. Photonics* **8**, 145 (2014).
- [7] T. J. Kippenberg, A. L. Gaeta, M. Lipson, and M. L. Gorodetsky, Dissipative Kerr solitons in optical microresonators, *Science* **361**, eaan8083 (2018).
- [8] H. Bao, A. Cooper, M. Rowley, L. Di Lauro, J. S. Toterogongora, S. T. Chu, B. E. Little, G.-L. Oppo, R. Morandotti, D. J. Moss, B. Wetzel, M. Peccianti, and A. Pasquazi, Laser cavity-soliton microcombs, *Nat. Photonics* **13**, 384 (2019).
- [9] M. Piccardo, B. Schwarz, D. Kazakov, M. Beiser, N. Opacak, Y. Wang, Sh. Jha, J. Hillbrand, M. Tamagnone, W. T. Chen, A. Y. Zhu, L. L. Columbo, A. Belyanin, and F. Capasso, Frequency combs induced by phase turbulence, *Nature (London)* **582**, 360 (2020).
- [10] M. Rowley, P.-H. Hanzard, A. Cutrona, H. Bao, S. T. Chu, B. E. Little, R. Morandotti, D. J. Moss, G.-L. Oppo, J. S. T. Gongora, M. Peccianti, and A. Pasquazi, Self-emergence of robust solitons in a microcavity, *Nature (London)* **608**, 303 (2022).
- [11] P. Marin-Palomo, J. N. Kemal, M. Karpov, A. Kordts, J. Pfeifle, M. H. P. Pfeiffer, P. Trocha, S. Wolf, V. Brasch, M. H. Anderson, R. Rosenberger, K. Vijayan, W. Freude, T. J. Kippenberg, and C. Koos, Microresonator-based solitons for massively parallel coherent optical communications, *Nature (London)* **546**, 274 (2017).
- [12] M.-G. Suh and K. J. Vahala, Soliton microcomb range measurement, *Science* **359**, 884 (2018).
- [13] A. Pasquazi, M. Peccianti, L. Razzari, D. J. Moss, S. Coen, M. Erkintalo, Y. K. Chembo, T. Hansson, S. Wabnitz, P. Del'Haye, X. Xue, A. M. Weiner, and R. Morandotti, Micro-combs: A novel generation of optical sources, *Phys. Rep.* **729**, 1 (2018).
- [14] T. Fortier and E. Baumann, 20 years of developments in optical frequency comb technology and applications, *Commun. Phys.* **2**, 153 (2019).
- [15] K. J. Vahala, Optical microcavities, *Nature (London)* **424**, 839 (2003).
- [16] T. Tanabe, S. Fujii, and R. Suzuki, Review on microresonator frequency combs, *Jpn. J. Appl. Phys.* **58**, SJ0801 (2019).
- [17] T. E. Drake, J. R. Stone, T. C. Briles, and S. B. Papp, Thermal decoherence and laser cooling of Kerr microresonator solitons, *Nat. Photonics* **14**, 480 (2020).
- [18] V. Brasch, M. Geiselmann, M. H. P. Pfeiffer, and T. J. Kippenberg, Bringing short-lived dissipative Kerr soliton states in microresonators into a steady state, *Opt. Express* **24**, 29312 (2016).
- [19] A. Kasapi, M. Jain, G. Y. Yin, and S. E. Harris, Electromagnetically induced transparency: Propagation dynamics, *Phys. Rev. Lett.* **74**, 2447 (1995).
- [20] L. V. Hau, S. E. Harris, Z. Dutton, and C. H. Behroozi, Light speed reduction to 17 metres per second in an ultracold atomic gas, *Nature (London)* **397**, 594 (1999).
- [21] D. F. Phillips, A. Fleischhauer, A. Mair, R. L. Walsworth, and M. D. Lukin, Storage of light in atomic vapor, *Phys. Rev. Lett.* **86**, 783 (2001).
- [22] C. Liu, Z. Dutton, C. H. Behroozi, and L. V. Hau, Observation of coherent optical information storage in an atomic medium using halted light pulses, *Nature (London)* **409**, 490 (2001).
- [23] Y.-F. Xiao, L. He, J. Zhu, and L. Yang, Electromagnetically induced transparency-like effect in a single polydimethylsiloxane-coated silica microtoroid, *Appl. Phys. Lett.* **94**, 231115 (2009).
- [24] Y.-C. Liu, B.-B. Li, and Y.-F. Xiao, Electromagnetically induced transparency in optical microcavities, *Nanophotonics* **6**, 789 (2017).
- [25] M. Fleischhauer, A. Imamoglu, and J. P. Marangos, Electromagnetically induced transparency: Optics in coherent media, *Rev. Mod. Phys.* **77**, 633 (2005).
- [26] H. Qin, M. Ding, and Y. Yin, Induced transparency with optical cavities, *Adv. Photonics Res.* **1**, 2000009 (2020).
- [27] L. Gu, H. Fang, J. Li, L. Fang, S. J. Chua, J. Zhao, and X. Gan, A compact structure for realizing Lorentzian, Fano, and electromagnetically induced transparency resonance lineshapes in a microring resonator, *Nanophotonics* **8**, 841 (2019).
- [28] G.-L. Oppo, Complex spatial structures due to atomic coherence, *J. Mod. Opt.* **57**, 1408 (2010).
- [29] M. Eslami, R. Kheradmand, D. McArthur, and G.-L. Oppo, Complex structures in media displaying electromagnetically induced transparency: Pattern multistability and competition, *Phys. Rev. A* **90**, 023840 (2014).
- [30] M. Eslami, M. Khanmohammadi, R. Kheradmand, and G.-L. Oppo, Optical turbulence and transverse rogue waves in a cavity with triple-quantum-dot molecules, *Phys. Rev. A* **96**, 033836 (2017).
- [31] M. Eslami, R. Kheradmand, and G.-L. Oppo, Complex structures in cavities with media displaying EIT: Coexistence, defects and selection mechanism, *J. Phys. B: At. Mol. Opt. Phys.* **53**, 075402 (2020).
- [32] M. Eslami and G.-L. Oppo, Nonlinear dynamics of triple quantum dot molecules in a cavity: Multi-stability of three types of cavity solitons, *Eur. Phys. J. D* **75**, 125 (2021).
- [33] M. Eslami, M. Kanafchian, G.-L. Oppo, Oscillatory and chaotic regimes of patterns and dark cavity solitons in cavities displaying EIT: Static multistable dual chimera states, *Chaos Solitons & Fractals* **167**, 113080 (2023).
- [34] G.-L. Oppo, D. Grant, and M. Eslami, Temporal cavity solitons and frequency combs via quantum interference, *Phys. Rev. A* **105**, L011501 (2022).
- [35] N. V. Vitanov, A. A. Rangelov, B. W. Shore, and K. Bergmann, Stimulated Raman adiabatic passage in physics, chemistry, and beyond, *Rev. Mod. Phys.* **89**, 015006 (2017).
- [36] A. Joshi, A. Brown, H. Wang, and M. Xiao, Controlling optical bistability in a three-level atomic system, *Phys. Rev. A* **67**, 041801(R) (2003).
- [37] M. Haelterman, S. Trillo, and S. Wabnitz, Dissipative modulation instability in a nonlinear dispersive ring cavity, *Opt. Commun.* **91**, 401 (1992).
- [38] A. S. Manka, H. M. Doss, L. M. Narducci, P. Ru, and G.-L. Oppo, Spontaneous emission and absorption properties of a driven three-level system. II. The  $\wedge$  and cascade models, *Phys. Rev. A* **43**, 3748 (1991).
- [39] C. Weber, B. Batagelj, P. Fiala, D. Auth, U. Dragonja, Q. Gaimard, A. Ramdane, and S. Breuer, Quantum dash frequency comb laser stabilisation by optical self-injection provided by an all-fibre based delay-controlled passive external cavity, *Electron. Lett.* **55**, 1006 (2019).
- [40] J. E. Cunningham, I. Shubin, X. Zheng, T. Pinguet, A. Mekis, Y. Luo, H. Thacker, G. Li, Jin Yao, K. Raj, and A. V.

- Krishnamoorthy, Highly-efficient thermally-tuned resonant optical filters, *Opt. Express* **18**, 19055 (2010).
- [41] L. A. Fuderer, L. Wang, J. S. Stuart, M. P. Hedges, A. G. Truscott, and S. S. Hodgman, In-fibre temperature tuned fibre ring resonator for laser mode monitoring, *Optics Continuum* **1**, 306 (2022).
- [42] N. N. Rosanov, *Spatial Hysteresis and Optical Patterns* (Springer, Berlin, 2002).
- [43] B. Garbin, Y. Wang, S. G. Murdoch, G.-L. Oppo, S. Coen, and M. Erkintalo, Experimental and numerical investigations of switching wave dynamics in a normally dispersive fibre ring resonator, *Eur. Phys. J. D* **71**, 240 (2017).
- [44] B. Garbin, J. Fatome, G.-L. Oppo, M. Erkintalo, S. G. Murdoch, and S. Coen, Dissipative polarization domain walls in a passive coherently driven kerr resonator, *Phys. Rev. Lett.* **126**, 023904 (2021).
- [45] G.-L. Oppo, A. J. Scroggie, and W. J. Firth, From domain walls to localized structures in degenerate optical parametric oscillators, *J. Opt. B: Quantum Semiclass. Opt.* **1**, 133 (1999).
- [46] G.-L. Oppo, A. J. Scroggie, and W. J. Firth, Characterization, dynamics and stabilization of diffractive domain walls and dark ring cavity solitons in parametric oscillators, *Phys. Rev. E* **63**, 066209 (2001).
- [47] X. Xue, Y. Xuan, Y. Liu, P. H. Wang, S. Chen, J. Wang, D. E. Leaird, M. Qi, A. M. Weiner, Mode-locked dark pulse Kerr combs in normal-dispersion microresonators, *Nat. Photonics* **9**, 594 (2015).
- [48] P. Parra-Rivas, D. Gomila, E. Knobloch, S. Coen, and L. Gelens, Origin and stability of dark pulse Kerr combs in normal dispersion resonators, *Opt. Lett.* **41**, 2402 (2016).
- [49] P. Parra-Rivas, E. Knobloch, D. Gomila, and L. Gelens, Dark solitons in the Lugiato-Lefever equation with normal dispersion, *Phys. Rev. A* **93**, 063839 (2016).
- [50] M. Gilles, P.-Y. Bony, J. Garnier, A. Picozzi, M. Guasoni, and J. Fatome, Polarization domain walls in optical fibres as topological bits for data transmission, *Nat. Photonics* **11**, 102 (2017).
- [51] C. Mas Arabí, P. Parra-Rivas, T. Hansson, L. Gelens, S. Wabnitz, and F. Leo, Localized structures formed through domain wall locking in cavity-enhanced second-harmonic generation, *Opt. Lett.* **45**, 5856 (2020).
- [52] M. Yu, Y. Okawachi, A. G. Griffith, M. Lipson, and A. L. Gaeta, Mode-locked mid-infrared frequency combs in a silicon microresonator, *Optica* **3**, 854 (2016).
- [53] K. Bergmann *et al.*, Roadmap on STIRAP applications, *J. Phys. B: At. Mol. Opt. Phys.* **52**, 202001 (2019).
- [54] Sh. Zhang, J. M. Silver, L. Del Bino, F. Copie, M. T. M. Woodley, G. N. Ghalanos, A. Svela, N. Moroney, and P. Del'Haye, Sub-milliwatt-level microresonator solitons with extended access range using an auxiliary laser, *Optica* **6**, 206 (2019).
- [55] A. G. Vladimirov, J. M. McSloy, D. V. Skryabin, and W. J. Firth, Two-dimensional clusters of solitary structures in driven optical cavities, *Phys. Rev. E* **65**, 046606 (2002).
- [56] Z. Lu, H.-J. Chen, W. Wang, L. Yao, Y. Wang, Y. Yu, B. E. Little, S. T. Chu, Q. Gong, W. Zhao, X. Yi, Y.-F. Xiao, and W. Zhang, Synthesized soliton crystals, *Nat. Commun.* **12**, 3179 (2021).
- [57] W. J. Firth and A. J. Scroggie, Optical bullet holes: Robust controllable localized states of a nonlinear cavity, *Phys. Rev. Lett.* **76**, 1623 (1996).
- [58] T. Hansson and S. Wabnitz, Frequency comb generation beyond the Lugiato-Lefever equation: Multi-stability and super cavity solitons, *J. Opt. Soc. Am. B* **32**, 1259 (2015).
- [59] M. Anderson, Y. Wang, F. Leo, S. Coen, M. Erkintalo, and S. G. Murdoch, Coexistence of multiple nonlinear states in a tristable passive Kerr resonator, *Phys. Rev. X* **7**, 031031 (2017).
- [60] Y. V. Kartashov, O. Alexander, and D. V. Skryabin, Multi-stability and coexisting soliton combs in ring resonators: The Lugiato-Lefever approach, *Opt. Express* **25**, 11550 (2017).
- [61] T. Hansson, P. Parra-Rivas, and S. Wabnitz, Modeling of dual frequency combs and bistable solitons in third-harmonic generation, *Commun. Phys.* **6**, 59 (2023).
- [62] A. G. Vladimirov, Temporal cavity soliton interaction in passively mode-locked semiconductor lasers, *Optics* **4**, 433 (2023).